JOURNAL OF SPACECRAFT AND ROCKETS
Vol. 29, No. 3, May-June 1992

Impact Damage and Residual Tension Strength of a Thick Graphite/Epoxy Rocket Motor Case

C. C. Poe Jr.*
NASA Langley Research Center, Hampton, Virginia 23665

Impacters of various masses were dropped from various heights onto thick graphite/epoxy filament-wound cylinders. The cylinders represented filament-wound cases (FWC) made for the booster motors of the Space Shuttle. Tups of various shapes were affixed to the impacters. Some of the cylinders were filled with inert propellant, and some were empty. The cylinders were impacted numerous times around the circumference and then cut into tension coupons, each containing an impact site. The size of the damage and the residual tension strength were measured. For hemispherical tups, strength was reduced as much as 30% by nonvisible damage. The damage consisted of matrix cracking and broken fibers. Analytical methods were used to predict the damage and residual tension strength. A factor of safety to account for nonvisible damage was determined. For corner and rod shaped tups, any damage that resulted in strength loss was readily visible. This paper is a summary of that work.

Nomenclature

a = depth of impact damage below surface or depth of equivalent surface crack, m
A_{11}, A_{22}, A_{12} = constants in Hertz's equation, Pa
c = half-length of impact damage in laminate plane or half-length of equivalent surface crack, m
E_1 = Young's modulus of impacter, Pa
E_{22} = Young's modulus of laminas normal to fiber direction, Pa
E_r, E_z = Young's moduli of transversely isotropic body, Pa
$f(a/h, a/c, c/w, \phi)$ = functional in stress intensity factor equation
F = impact or contact force, N
F_{max} = maximum impact or contact force, N
F_{tu} = undamaged tension strength, MPa
G_{xy}, G_{zx} = shear moduli of laminate, Pa
G_{zr} = shear modulus of transversely isotropic body, Pa
G_{12} = shear modulus of laminas, Pa
h = thickness, m
k_b = spring constant for beam deflection, N/m
k_1, k_2 = constants in Hertz's equation, Pa
K_Q = critical stress intensity factor or fracture toughness, $Pa\sqrt{mm}$
KE_{eff} = effective kinetic energy, $\frac{1}{2}Mv_1^2$, J
m_1, m_2 = mass of impacter and composite ring (including propellant), respectively, kg
M = effective mass, kg
n_0 = factor in Hertz's equation, Pa
p = contact pressure, Pa
p_c = average contact pressure, Pa
Q = shape factor for an elliptical crack
r_c = contact radius, m
R_1 = radius of impacter, m
S_{xf} = gross laminate stress in hoop direction for failure of first ligament, Pa
u = relative displacement between impacter and composite ring, m
u_b = beam type (global) displacement of composite ring, m
u_i = local displacement (indentation) of composite ring given by Hertz's equation, m
v_1 = velocity of impacter, m/s
w = width of specimen in test section, m
ν = Poisson's ratio of an isotropic material
ν_1 = Poisson's ratio of impacter
ν_{12} = principal Poisson's ratio of lamina
ν_r, ν_{rz} = Poisson's ratios of transversely isotropic semi-infinite body
$\nu_{xy}, \nu_{yx}, \nu_{xz}, \nu_{yz}$ = Poisson's ratios of laminate
σ_{cu} = compression strength, Pa
τ_u = shear strength, Pa
ϕ = parametric angle of ellipse

Subscripts

r, θ, z = cylindrical coordinates, z direction is normal to the laminate
x, y = Cartesian coordinates, x direction is the axial direction of the cylinder or hoop direction of the filament wound case laminate
1,2 = principal coordinates of laminas, 1 direction is the fiber direction

Original measurements were made in customary units and converted to SI units.

Introduction

BEFORE the loss of the Space Shuttle Challenger, NASA initiated a program to develop and build several sets of booster motors with graphite/epoxy cases for the Space Shuttle to be used in lieu of existing motors with steel cases. These lightweight motors were to have been used for certain Air Force missions from a new launch facility being constructed at Vandenburg Air Force Base. However, construction of the new launch facility was canceled, causing NASA to cancel development of the new motors. Nevertheless, research on

Received July 20, 1990; revision received Jan. 5, 1991; accepted for publication Feb. 27, 1991.

*Director for Structures, Mail Stop 188E.

damage tolerance yielded generic information for other applications of thick composites to motor cases and other structures. The primary contractor was Morton Thiokol Inc. The graphite/epoxy cases were made by Hercules using a wet filament-winding process, hence the name filament-wound case (FWC). It was desired, but not required, that the FWCs be reusable like the steel cases. Each lightweight motor consisted of four FWCs: a forward case, two center cases, and an aft case. The FWCs were 3.66 m in diameter and were joined together with steel pins. The forward and center FWCs were 7.6 m in length, and the aft FWC was somewhat shorter. The thickness of the membrane region away from the ends was approximately 36 mm. The ends were thicker to withstand the concentrated pin loads. The FWCs were designed primarily for internal pressure caused by the burning propellant.

The burst pressure of graphite/epoxy pressure vessels with thin walls has been shown to be reduced significantly by low-velocity impacts.[1] However, it was not known if low-velocity impacts could seriously reduce the strength of pressure vessels with thick walls such as the FWCs. Therefore, an investigation was made to determine the damage and reduction in tension strength caused by low-velocity impacts. It was not economically feasible to pressure test actual FWCs for the number of parameters to be studied. Thus, a 36-mm-thick cylinder was made to represent an FWC. The cylinder was 2.13 m long and 76.2 cm in diameter. Following ultrasonic inspection, the cylinder was cut into seven rings (short cylinders) that were 30.5 cm long. The hoop and helical fiber directions of the cylinder were rotated 90 deg relative to those of the FWC to provide straight specimens for uniaxial tension loading in the hoop direction, the most highly stressed direction. Otherwise, uniaxial load could not be applied in the hoop direction without causing bending of the laminate, which would be unrepresentative of an FWC with internal pressure. Thus, the hoop layers of the FWCs became longitudinal layers in the cylinder. (In this paper, all references to hoop direction are to the long direction of the cylinder.) The helical layers of the cylinder were wet wound, but the longitudinal layers could not be wound on the equipment available and had to be laid by hand using unidirectional prepreg tape.

It was originally believed that the propellant could be simulated in impact tests by cutting the rings into 51-mm-wide by 30.5-cm-long tension specimens, placing a specimen on a large block of inert propellant, and then dropping an impacter onto the specimen.[2,3] However, preliminary tests revealed that the propellant acted as a cushion to reduce the impact force rather than as additional mass to increase the impact force. For this reason, it was decided to drop the impacters onto the rings and then cut tension specimens from the rings. To determine the actual effect of the propellant, some of the rings were filled with inert propellant. For a given impact force, it was believed that the damage in the rings would be the same as that in an FWC because the lay-up and thickness of the rings and the FWCs were the same. Also, for given damage, it was assumed that the hoop stress at failure for an FWC with internal pressure and the strength of a uniaxially loaded specimen would be equal.

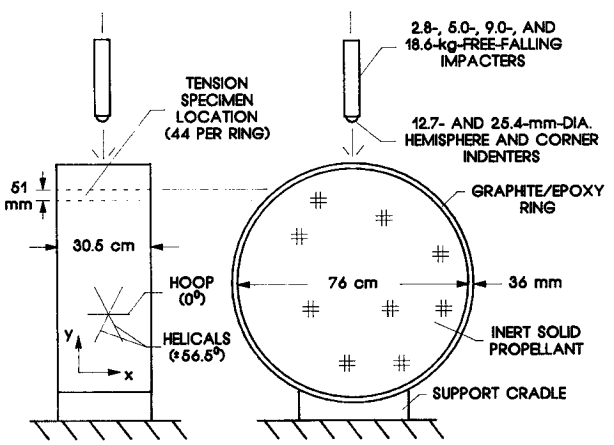

Fig. 1 Impact tests of graphite/epoxy rings.

In the first series of impact tests on the rings, a 25.4-mm-diam hemisphere was used for the indenter (tup).[4-6] The impacters were of various masses and were dropped from various heights to simulate falling tools and equipment. The specimens were radiographed before being loaded to failure. The extent of impact damage increased with increasing impact force, and the residual tension strength decreased accordingly. For impact forces around 76 kN, strengths were reduced as much as 30% without damage being readily visible on the surface. The resin was removed from several specimens following impact, revealing broken fibers. The locus of the broken fibers resembled cracks on a macroscopic scale. The damage size (breadth and depth) was calculated assuming Hertzian contact and maximum stress criteria. The damage was represented as a surface crack, and residual tension strength was calculated using surface crack analysis.[6,7] The predictions and experiments were in reasonably good agreement. The size and nature of the damage were difficult to determine nondestructively.[3,8-10] Thus, a number of specimens were damaged by simulated impacts and deplied to verify the predictions of damage.[11] The impacts were simulated by quasistatically pressing the indenter against the face of specimens that had been cut from an actual FWC. These measurements of damage size were also in good agreement with calculations made assuming Hertzian contact and maximum stress criteria.

Because of concern about reduction in strength due to nonvisible impact damage, additional impact tests were conducted on the remaining filled and empty rings to determine the relevance of impacter shape to nonvisible damage and the associated reduction in strength.[12] The following indenters were used: a 12.7-mm-diam hemisphere, a sharp corner, and a 6.3-mm-diam bolt-like rod. Only the height from which the impacter was dropped was varied, not the mass. Because no rings remained, impacts with the rod were simulated by quasistatically pressing the rod against the face of specimens that had been cut earlier from an empty ring. The specimens were then loaded uniaxially in tension to failure. The effects of indenter shape on impact force, damage size, damage visibility, and residual tensile strength were calculated using the previously developed analyses.[4-6] Factors of safety for strength reduction with nonvisible damage were calculated in terms of impact energy.

Although this investigation was made using uniaxially loaded specimens, an actual FWC with damage and delaminations in critical locations was pressure tested to failure by Hercules at the end of the program. Those results are summarized and compared with the present results.

Certain commercial materials are identified in this paper to specify adequately which materials were used. In no case does such identification imply that the materials are necessarily the only ones or the best ones available for the purpose.

Experiments

The material, test apparatus, and procedure have been described in detail elsewhere.[2,4-6,11,12] They will also be reviewed here for the convenience of the reader.

Material

The 0.76-m-diam, 2.13-m-long cylinder was made by Hercules Inc. to represent the membrane region of an FWC. The thickness of the cylinder was the same as that of an FWC, 36 mm. The hoop and helical fiber directions of the cylinder were rotated 90 deg relative to those of the FWC to provide straight specimens for uniaxial loading in the hoop direction of the FWC. The directions of the hoop (0 deg) and helical (± 56.5 deg) layers are shown in Fig. 1 for the cylinder.

Table 1 Elastic constants of FWC

Property	Value
E_x, GPa	30.6
E_y, GPa	39.0
E_z, GPa	4.15
G_{xy}, GPa	19.7
G_{zx}, GPa	4.38
ν_{xy}	0.351
ν_{yx}	0.447
ν_{xz}	0.271
ν_{xz}	0.271

(The 0-deg and ±56.5-deg directions are measured relative to the longitudinal direction of the cylinder.) From outside to inside, the orientations of the layers were

$$\{(\pm 56.5)_2/0/[(\pm \underline{56.5})_2/0]_3/[(\pm 56.5)_2/0]_7/(\pm 56.5/0_2)_4$$

$$/(\pm 56.5)_2/(0/90)_c\}$$

where the underlined helical layers are about 1.6 times as thick as the other helical layers and $(0/90)_c$ is a plane weave cloth at the inner surface.

The ±56.5-deg layers were filament wound using a wet process. The fibers and winding resin were Hercules Inc.'s AS4W-12K graphite and HBRF-55A epoxy, the same as those of the FWCs. The 0-deg layers could not be filament wound with the available equipment; instead, they were laid by hand using prepreg tape made of the same fibers and a compatible epoxy, Hercules Inc.'s MX-16. The elastic constants of the laminate, which were calculated using lamination theory, are given in Table 1. The x and y directions in the subscripts of the elastic constants correspond to the axial and hoop directions of the cylinder, respectively (see Fig. 1). The z direction corresponds to the radial direction of the cylinder or FWC.

Inert solid propellant was cast into some of the rings. The masses of an empty and a filled ring were 40 and 288 kg, respectively.

Test Apparatus and Procedure

Impact Tests

The rings were impacted by free-falling masses (see Fig. 1). During impacts, the rings lay on a thin rubber sheet in a shallow aluminum cradle. The bottom of the empty rings was secured to the concrete floor with a crossbar to prevent the rings from "leaping" off the floor when impacted. Each ring was impacted every 59 mm of outer circumference, giving 44 impact sites. The damaged regions did not overlap. Some sites on each ring were not impacted but reserved as undamaged specimens for determining mechanical properties. The cut edges of each specimen were ground flat and parallel so that the width and length of the specimens were 51 mm and 31 cm, respectively. The center of each specimen was made to coincide with an impact site.

The free-falling impacters were 51-mm-diam steel rods with indenters of various shapes attached to one end. Four rods of different lengths were used to give masses of 2.8, 5.0, 9.0, and 18.6 kg, including the indenter. A piezoelectric accelerometer and four strain gauges were embedded in the rods immediately behind the indenter for measuring acceleration and impact force, respectively. The indenters were a 12.7- and a 25.4-mm-diam hemisphere and a corner made of three orthogonal surfaces. The tip of the corner had a radius of about 0.25 mm.

For the 25.4-mm-diam hemisphere, impacters of the four masses were dropped on one empty and one filled ring. Drop heights were varied to give kinetic energies from 41 to 446 J. The contact area was recorded by placing sheets of white bond paper and carbon paper on the rings. For the 12.7-mm-diam hemisphere and the corner, the 5.0-kg impacter was dropped on one empty and one filled ring. Drop heights were varied from 36 to 274 cm to give kinetic energies from 17 to 136 J.

Simulated Impact Tests

Because of a lack of whole rings, some impact tests were simulated by slowly pressing indenters against the face of small specimens while controlling the magnitude of the force. The impacts were not made by dropping weights because of a potential difference between the dynamic response of the ring and that of a small specimen. The force was applied with a 500-kN servo-controlled, hydraulic testing machine. The indenters were attached to one grip of the testing machine, and the specimens lay on a steel platen attached to the other grip.

In the first case, simulated impact tests were conducted on 30.5×30.5-cm FWC pieces to better determine the nature of the fiber damage and to verify predictions of damage size. The pieces were from an FWC that had essentially the same lay-up as the cylinder but was completely wet-wound with AS4W-12K graphite and HBRF-55A epoxy. Thirty-six 38×38-mm specimens were cut from each FWC piece after the forces were applied. The contact sites were at the center of the specimens. The specimens were heated to 400°C for 60 min to remove most of the epoxy. Following pyrolysis, the layers were separated and examined with an optical microscope to measure the extent of fiber damage. Hemispherical indenters of three diameters were used: 12.7, 25.4, and 50.8 mm. The average contact pressure to cause visible surface damage was about 648 MPa. Thus, contact pressures were selected between 408 and 742 MPa so that maximum nonvisible damage was included. The corresponding forces, which were calculated assuming Hertzian contact, varied from 4.18 to 400 kN. The smallest force corresponds to the smallest indenter and the largest to the largest indenter.

In the second case, nine of the 51×30.5-cm tension specimens that were reserved for tests to determine mechanical properties were used instead for simulated impact tests with a rod-shaped indenter. The rod had a diameter of 6.3 mm. The corner of the rod (intersection of the side and end) had a radius of 1.3 mm to simulate the end of a bolt. Stroke (displacement of the indenter) was programmed to increase linearly with time. The maximum strokes were 3.4, 6.5, and 9.5 mm for three specimens each.

X-Ray Tests

The impacted face of each specimen (including those with simulated impacts using the rod) was soaked in a zinc iodide penetrant for 30 s, and radiographs were made from the impacted side and the edge. The penetrant was contained by a circular dam on the surface of the specimen. The depth of impact damage in the radiographs was measured. The pieces from the FWC that were subjected to simulated impacts and deplied were not radiographed.

Residual Strength Tests

After the specimens were x-rayed, circular arcs were ground into the specimens' edges to reduce the width in the test section to 33 or 38 mm (see Fig. 2). The specimens were uniaxially

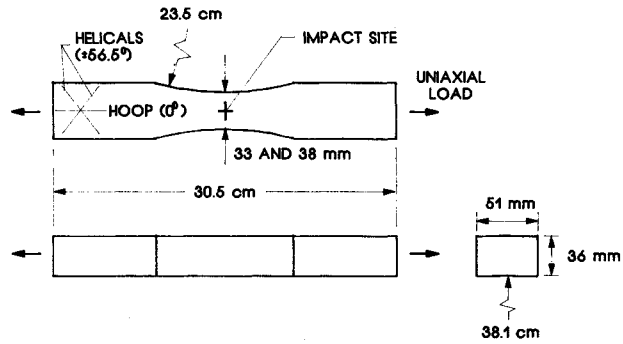

Fig. 2 Tension specimen.

loaded to failure in tension with a 445-kN capacity hydraulic testing machine. Stroke was programmed to increase with time at the rate of 0.0076 mm/s. Time to failure was several minutes at this rate. Hydraulically actuated grips that simulate fixed-end conditions were used. Otherwise, uniaxial loading would cause bending because the FWC laminate is not symmetrical. Strain gauges verified that bending strains were relatively small compared to the axial strains. To hold onto the specimens, the grips generated very high contact pressure on the faces of the specimens. Without reducing the width in the test section, the failure of specimens with small damage appeared to originate at the edge of the grips where the contact pressure was highest.

Results

The mass of a ring filled with inert solid propellant was about seven times that of an empty ring. An effective kinetic energy parameter was derived that takes into account the mass of the target as well as that of the impacter. The first part of the results section verifies this parameter.

Hertzian Contact

For Hertzian contact between an isotropic sphere and a transversely isotropic semi-infinite body,[13] the contact radius is

$$r_c = (FR_1/n_0)^{1/3} \tag{1}$$

where R_1 is the radius of the sphere, F is the contact force, and n_0 is a function of the elastic constants of the sphere and semi-infinite body given by Eq. (A1) in the Appendix.

The local displacement or indentation of the semi-infinite body is

$$u_i = R_1^{-1/3}(F/n_0)^{2/3} \tag{2}$$

Equation (2) is accurate only when $u_i \ll R_1$.

During the time that the impacter and target are in contact, the impact force F increases with time to a maximum value F_{max} and then decreases to zero, much as a haversine. Of course, the impact-force time history also contains high-frequency, low-amplitude oscillations associated with vibrations of the target and impacter. The duration of the impact and hence the time for the impact force to reach a maximum value increases with increasing impacter mass. For the filled and empty rings, the duration varied between 1 and 2 ms for the range of impacter masses. The measurements of contact diameter are plotted against F_{max} in Fig. 3 for the 25.4-mm-diam hemisphere. Different symbols were used to differentiate between the filled and empty rings and to indicate when indenters made visible impressions or craters. Hereafter, visible indenter impressions will be referred to as visible damage. Depth of impressions was not measured; instead, the judgment as to

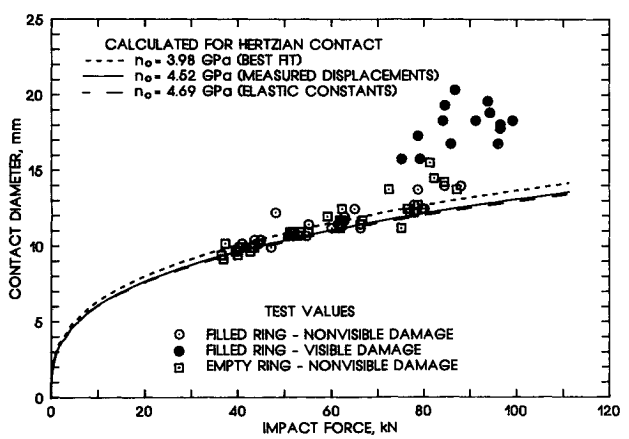

Fig. 3 Contact diameter vs impact force for 25.4-mm-diam hemisphere.

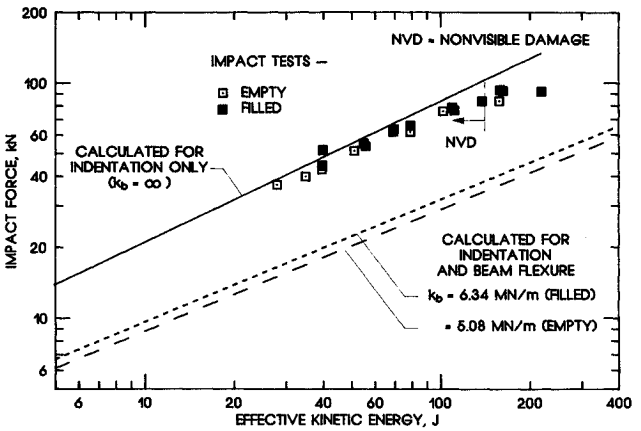

Fig. 4 Impact force vs effective kinetic energy for 25.4-mm-diam hemisphere.

which impressions were visible was solely subjective. For the empty ring, contact area was inadvertently not recorded for the impacts that made visible damage. For $F_{max} < 75$ kN, the damage was not visible. For F_{max} slightly above 75 kN, the impressions were very shallow but perceptible. The depth of the impressions increased with increasing F_{max}. Equation (1) is also plotted in Fig. 3 for three different values of n_0: one value calculated with Eq. (A1) using the elastic constants in Table 1, another calculated with Eq. (2) using measured displacements of the FWC pieces that were subjected to simulated impacts, and one calculated to best fit the measurements of contact diameter without visible damage. In using Eq. (A1) to calculate n_0, transversely isotropic properties were calculated by averaging the x and y direction properties in Table 1. The curves and test data without visible damage agree quite well. When the impacts made visible damage, the contact diameter is underestimated by Eq. (1).

Relationship Between Mass, Velocity, and Impact Force

Assuming Hertzian contact and Newtonian mechanics, the following relationship was derived between the maximum impact force, impacter mass, composite ring mass, and impacter velocity[12]:

$$\frac{1}{2}k_b^{-1}F_{max}^2 + \frac{2}{5}R_1^{-1/3}n_0^{-2/3}F_{max}^{5/3} - KE_{eff} = 0 \tag{3}$$

The composite ring was assumed to be initially at rest. The term KE_{eff} is the effective kinetic energy defined by

$$KE_{eff} = \tfrac{1}{2}Mv_1^2 \tag{4}$$

and M is the effective mass defined by

$$M = \left[m_1^{-1} + (m_2/4)^{-1}\right]^{-1} \tag{5}$$

where v_1 is the velocity of the impacter, m_1 is the mass of the impacter, and $m_2/4$ is the effective mass of the ring (including the propellant). The effective mass of the rings were determined using rebound velocities. The relative displacement of the ring and impacter was written as

$$u = u_b + u_i \tag{6}$$

where u_i is the local displacement of the ring defined by Eq. (2) and u_b is the beam type displacement of the ring defined by

$$u_b = F/k_b \tag{7}$$

Measured values of F_{max} are plotted against KE_{eff} in Fig. 4 for the 25.4-mm-diam hemisphere. Each symbol is an average of several tests. The threshold value of KE_{eff} for nonvisible

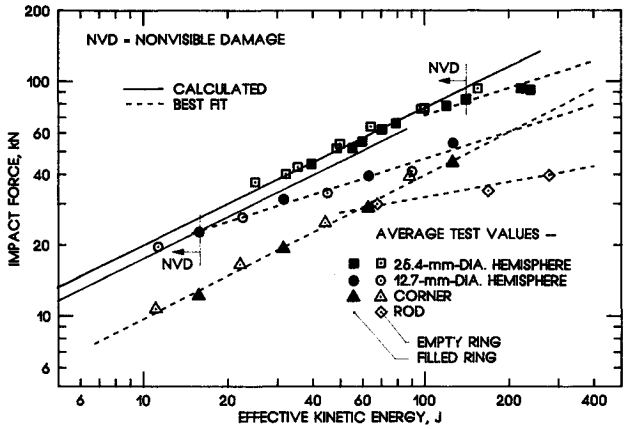

Fig. 5 Effect of impacter shape on impact force.

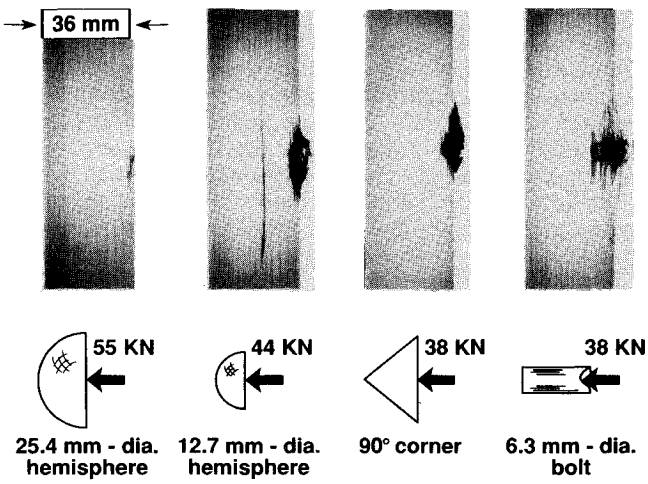

Fig. 6 Radiographs of impact damage for various indenters.

damage is labeled. The values of F_{max} for the empty and filled rings coalesce quite well for the same value of KE_{eff}. Values of F_{max} calculated with Eq. (3) and $n_0 = 4.52$ GPa are also plotted. Curves are shown for three values of ring stiffness: $k_b = \infty$, 6.34 MN/m, and 5.08 MN/m. For $k_b = \infty$, the ring does not deflect in a global sense as a beam. The last two values of k_b were measured by quasistatically pressing the hemisphere against a filled ring and an empty ring, respectively. When the damage was not visible, the calculated curve for $k_b = \infty$ agrees with the test results quite well. But when damage was visible, the actual impact forces are less than the calculated values, and the difference increases with increasing KE_{eff}. Values of F_{max} calculated with the quasistatic values of k_b are much too small.

Displacements are smaller when forces are applied dynamically than when they are applied quasistatically. The duration of impact decreased with decreasing mass of the impacter and was relatively independent of velocity of the impacter.[4,5] For the filled and empty rings, the impact durations were very short, 1 to 2 ms for the range of impacter masses. Thus, time was not sufficient for global displacements to develop, and the quasistatic values of k_b greatly overestimated the global displacement of the rings during impact.

Values of F_{max} are plotted against KE_{eff} in Fig. 5 for the 12.7- and 25.4-mm-diam hemisphere, the corner, and the rod. For the simulated impacts with the rod, the area under the load-displacement curve was used for KE_{eff}. Each symbol is an average of several tests. Thresholds for nonvisible damage are indicated for the hemispheres. The corner and rod made visible damage in all tests. The dashed lines were fit to the test data with visible damage. Again the values of F_{max} for the empty and filled rings coalesce quite well for the same value of KE_{eff}.

For the hemispheres, F_{max} increases with increasing radius for a given KE_{eff}. For the range of KE_{eff} values investigated, values of F_{max} are lower for the corner and rod than for the hemispheres. After a critical force was exceeded, the rod acted like a punch and penetrated deeply into the composite. Because of the large displacements, the work increased rapidly with force. Thus, the slope of the test data for the rod is the smallest. Because of the corner's profile, the resistance to penetration increased rapidly with increasing penetration. Thus, the slope of the test data for the corner was as large as that for the hemispheres without visible damage. The solid lines for the hemispheres were calculated with Eq. (3). The calculations were made using $k_b = 219$ MN/m and $n_0 = 4.52$ GPa. This value of k_b was chosen to give the best agreement between Eq. (3) and the test data with nonvisible damage. Even though $k_b = 219$ MN/m is not ∞, it is still very large compared to the static values, and the term containing k_b in Eq. (3) contributes very little to KE_{eff}. The values of F_{max} calculated with Eq. (3) agree quite well with the test values for both hemispheres, when the damage is not visible. When the damage is visible, the calculated values of F_{max} are greater than the test values.

Damage

Radiographs (edge views) of damage for the various indenters are shown in Fig. 6. These impact tests were conducted early in the investigation when the specimens lay on inert propellent. These radiographs illustrate that indenter shape had a strong effect on the extent of the damage. The kinetic energy of the impacter was 272 J. The corresponding impact forces are shown for each indenter. These impact forces do not correspond closely to those for the ring tests for the same kinetic energy.

For impacts to the rings, the maximum depth of damage in radiographs is plotted against KE_{eff} in Fig. 7 for the hemispheres and corner. For the rod, the impacts were simulated, and the area under the load-displacement curve was used for KE_{eff}. Filled and empty symbols differentiate between filled and empty rings. Except for the 25.4-mm-diam hemisphere, the data for the filled and empty rings coalesce quite well for a given value of KE_{eff}. For the 25.4-mm-diam hemisphere, the data coalesce for the largest values of KE_{eff} but diverge with decreasing KE_{eff}. For small values of KE_{eff}, the damage was deeper in the empty ring than in the filled ring. For all indenters but the rod, the data also tend to coalesce for the largest values of KE_{eff}. Moreover, for values of $KE_{eff} > 200$ J, it appears that that damage could be deeper for the 25.4-mm-diam hemisphere than for the 12.7-mm-diam hemisphere and the corner. The threshold for nonvisible damage is also shown in Fig. 7 for the hemispheres. For the 12.7-mm-diam hemisphere, damage was visible on the surface whenever it was deeper than 0.5 mm. However, for the 25.4-mm-diam hemisphere, damage was not visible on the surface until it was deeper than 4.0 mm.

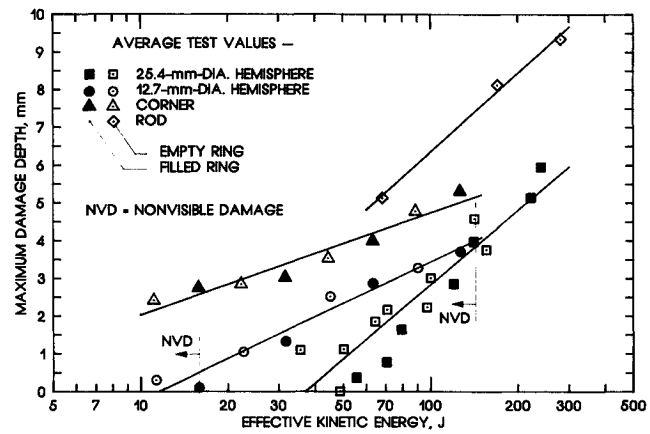

Fig. 7 Effect of impacter shape on maximum damage depth in radiographs.

Residual Tension Strength

When the impacted specimens were loaded to failure in tension, those with very shallow damage (outermost helical layers or less) failed catastrophically in one stage. But those with deeper damage (one or more hoop layers) failed in two stages: first, the damaged layers failed and delaminated from the undamaged layers (see Fig. 8); then, with additional load, the undamaged layers failed. The two stages of failure were referred to as first- and remaining-ligament failure.

Chatterjee[14] made calculations of the strain energy release rate for the delamination after failure of the first ligament and found that it was large relative to the interlaminar toughness of similar graphite/epoxy laminates. Thus, such a delamination would probably spread throughout a FWC as long as the internal pressure was not reduced.

The stresses for first- and remaining-ligament failure are plotted against KE_{eff} in Figs. 9 and 10 for the various indenters. For the rod, the area under the load-displacement curve was used for KE_{eff}. Filled and empty symbols are used to differentiate between the filled and empty rings. For a given value of KE_{eff} and indenter, the failure stresses do not coalesce as well as the values of $F_{\max}$ in Fig. 5. For the 25.4-mm-diam hemisphere, failure stresses were lower for the empty ring than for the filled ring. But for the 12.7-mm-diam hemisphere and the corner, failure stresses were lower for the filled ring than for the empty ring. Thus, the differences are inconsistent and not likely due to the presence of the inert propellent. Unexpectedly, the stresses for first- and remaining-ligament failure only vary 10–15% with indenter shape for a given value of KE_{eff}. For the two hemispheres, values of KE_{eff} for nonvisible damage are also shown in Figs. 9 and 10. The failure stresses associated with nonvisible damage decreased with increasing diameter. For the 25.4-mm-diam hemisphere, the stress for first-ligament failure with nonvisible damage was as low as 70% of the undamaged strength.

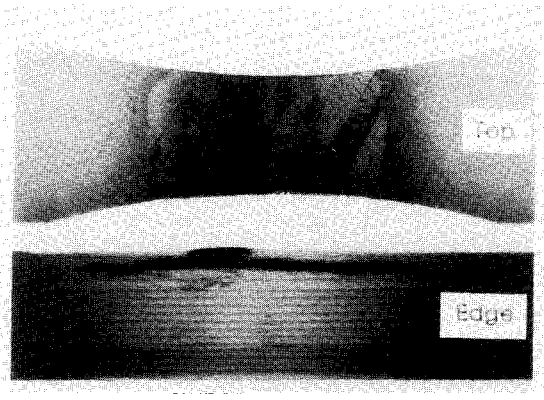

Fig. 8 Radiographs of tension specimen after failure of first ligament.

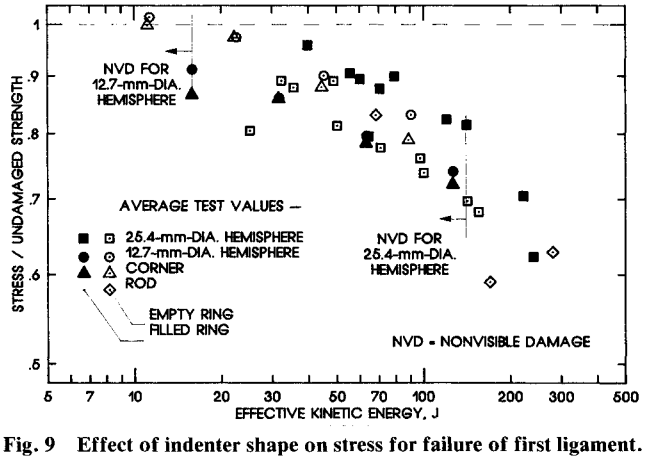

Fig. 9 Effect of indenter shape on stress for failure of first ligament.

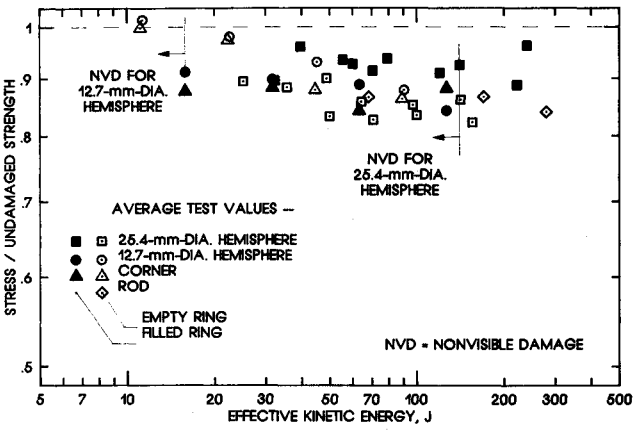

Fig. 10 Effect of indenter shape on stress for failure of remaining ligament.

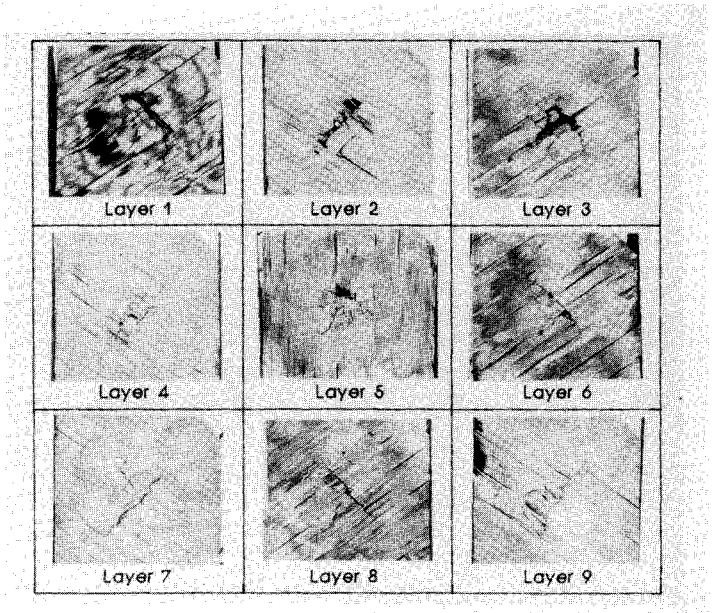

Fig. 11 Fiber damage in outermost nine layers.

Analysis and Discussion

Fiber Damage

Photographs of the outermost nine layers from a deplied specimen are shown in Fig. 11. This specimen is one of those taken from a piece of an actual FWC. It was subjected to a simulated impact using a 50.8-mm-diam hemisphere, producing a contact force of 267 kN. The layers contain broken fibers, the loci of which resemble cracks on a macroscale. Broken fibers were visible in the 15 outermost layers, of which the outermost 9 are shown here. The cracks are mostly parallel to the direction of fibers in the neighboring layers. When the direction of fibers on opposite sides of a layer were not equal, the direction of the cracks in the intermediate layer wandered between the direction of the fibers in the neighboring layers. Several specimens were not deplied but were sectioned normal to the plane of the laminate and examined using a scanning electron microscope.[11] The sections revealed matrix cracks in planes of maximum shear stress that passed through broken fibers. The ends of broken fibers were displaced relative to one another as though the fibers also broke in shear. Probably shear failure of the matrix precipitated the failure of the fibers.

The maximum depth of broken fibers divided by contact radius r_c are plotted against average contact pressure p_c in Fig. 12 for hemispherical indenters with three diameters: 12.7, 25.4, and 50.8 mm. The depths were determined from deplied specimens like that in Fig. 11. Values of r_c were calculated using Eq. (1) with $n_0 = 4.52$ MPa, and values of p_c were calcu-

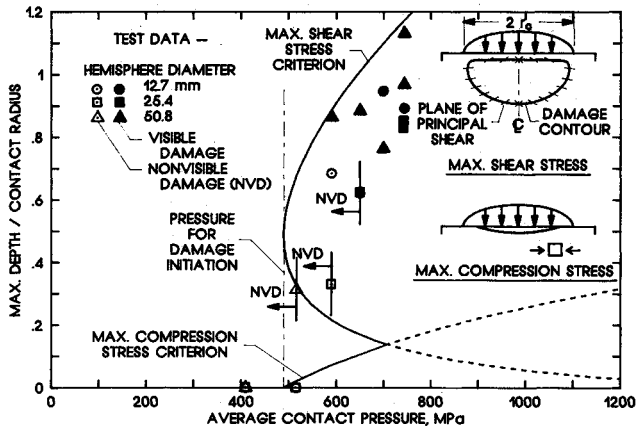

Fig. 12 Maximum damage depth vs contact pressure.

lated using $p_c = F_{max}/(\pi r_c^2)$. The filled and empty symbols distinguish between visible and nonvisible damage. The values of p_c for nonvisible damage decreased with increasing R_1.

Equation (1) can also be written

$$r_c = R_1 p_c/(\pi n_0) \tag{8}$$

Thus, r_c increases in proportion to R_1 for a given value of p_c, and the values of r_c for the smallest hemisphere are generally one-fourth those for the largest hemisphere. For this reason, the absolute depth of damage for the smallest hemisphere is generally one-fourth that for the largest hemisphere. This variation in damage size with R_1 may cause the decrease in p_c with increasing R_1 for nonvisible damage. That is, the size of surface damage, and hence the visibility of the damage, also decreases with decreasing R_1.

For impact tests with the 12.7- and 25.4-mm-diam hemispheres, the values of p_c for nonvisible damage were 719 MPa and 700 MPa, respectively. These values of p_c are only about 13% less than those in Fig. 12 for corresponding diameters. Also, damage depths in Figs. 7 and 12 are in reasonably good agreement, more so for the 25.4-mm-diam hemisphere than the 12.7-mm-diam hemisphere.[12]

For Hertzian contact between an isotropic sphere of radius R_1 and a semi-infinite transversely isotropic body,[13] the contact pressure on the surface of the semi-infinite body is given by

$$p = (3/2)\, p_c (1 - r^2/r_c^2)^{1/2} \tag{9}$$

where r is the radius measured from the center of the contact site (polar coordinate). Notice that the pressure at the center ($r = 0$) is 50% greater than the average value.

Using the theory of elasticity, Love[15] obtained a closed form solution for the internal stresses in a semi-infinite, isotropic body produced by the "hemispherical" pressure given by Eq. (9). Even though the composite is made of orthotropic layers, results from Love's solution should at least be applicable in a qualitative sense if r_c is much greater than the thickness of the layers. Damage contours were calculated with stresses from Love's solution, a maximum shear stress criterion, and a maximum compression stress criterion in the plane of the laminate. A compression allowable of $\sigma_{cu} = 587$ MPa, a shear allowable of $\tau_u = 228$ MPa, and a value of $\nu = 0.3$ were used. The compression allowable of 587 MPa was calculated by multiplying the compression failing strain by Young's modulus of the laminate. The shear allowable of 228 MPa was chosen to give an upper bound to the damage depths in Fig. 12. The plane of maximum shear stress varies along the damage contour. At the center ($r = 0$), the plane of maximum shear is at 45 deg to the plane of the laminate. (See the sketch in Fig. 12.) Near the extremity of the contact region ($r = r_c$), the plane of maximum shear stress is nearer the plane of the laminate. The maximum depths of the contours divided by r_c are plotted against p_c in Fig. 12. The values of r_c were calculated as were those of the test data. For the maximum shear stress criterion, the damage initiates below the surface at a depth of $0.482\, r_c$ when $p_c = 490$ MPa, which corresponds to $p_c = 2.15\, \tau_u$. For the maximum compression stress criterion, the damage initiates at the surface when $p_c = 487$ MPa, which corresponds to $p_c = 0.833\, \sigma_{cu}$. The envelope of the two maximum stress criteria is represented by the solid lines. The damage far below the surface corresponds to the maximum shear stress criterion, and the damage near the surface corresponds to the maximum compression stress criterion. The maximum stress criteria represent the data quite well considering that the composite is neither homogeneous nor isotropic. Widths of the calculated contours were approximately 1.6 times the depth, whereas those from the tests were 2 to 3 times the depth.[11] This discrepancy is probably due to the anisotropy the composite.

Transverse compression tests of disks of several diameters gave a value of $\tau_u = 310$ MPa, which is about 50% greater than that used to calculate the curve in Fig. 12. One would expect the value of τ_u from the compression tests to give values of damage depth that agree with the experimental values in Fig. 12 on the average. Instead, use of the larger value of τ_u would move the threshold from 490 to 668 MPa and give a lower bound to the test data. This discrepancy is likely due to the use of Love's isotropic solution to calculate internal stresses.

As noted previously, all impacts by the corner and rod caused visible damage on the surface. Contact pressures (averaged over the contact surface) for the corner and rod exceeded those for the hemispheres to cause visible damage, particularly the corner.[12] Thus, average contact pressure p_c may be a good indicator of damage initiation even though the maximum contact pressure varies with indenter shape. For example, Eq. (9) indicates that the maximum pressure for a hemisphere is 1.5 times the average and occurs at the center. But the contact pressure tends to be unbounded near the edge of a rod with a flat end. This unbounded pressure gives rise to unbounded stresses that cause a punch-type behavior.

Residual Tension Strength

The stresses for first-ligament failure are critical because they are either less than or equal to those for remaining-ligament failure. Thus, only the analysis of stresses for first-ligament failure will be reviewed. The impact damage was represented as a semi-elliptical surface crack, and the stress for failure of the first ligament was calculated using surface crack analysis.[4-7] The crack was assumed to be in a plane normal to the hoop direction. The depth of the equivalent crack a was calculated with stresses from Love's solution and the maximum shear stress criterion with $\tau_u = 228$ MPa and $n_0 = 4.52$ GPa. The length of the equivalent crack $2c$ was assumed to be two times the depth (semicircular). At failure, the critical stress intensity factor[16] or fracture toughness K_Q is given by

$$K_Q = S_{xf}(\pi a/Q)^{1/2} f(a/h, a/c, c/w, \phi) \tag{10}$$

where S_{xf} is the laminate stress for failure of the first ligament, Q is the shape function, and $f(a/h, a/c, c/w, \phi)$ is the correction factor for finite thickness h and width w. The parametric angle ϕ was taken as 0 or 90 deg, whichever gave the largest value of the correction factor. The fracture toughness K_Q of the laminate was calculated using the elastic constants, the failing strain of the fibers, and a general fracture toughness parameter.[4-6] For a crack whose plane is normal to the 0-deg direction of the cylinder, the result was $K_Q = 0.949$ GPa$\sqrt{\text{mm}}$.

For shallow surface cracks or impact damage, Eq. (10) gives strengths that are greater than those from tests. To correct this discrepancy, a line was drawn tangent to Eq. (10) and passing through the undamaged strength at a depth corresponding to the outermost hoop layer.[6] (Strengths were not reduced unless the hoop layers were damaged.)

Values of S_{xf} are plotted against KE_{eff} in Fig. 13 for the 12.7- and 25.4-mm-diam hemispheres. The values of S_{xf} were divided by the undamaged strength $F_{tu} = 345$ MPa. The open and filled symbols for the test data differentiate between visible and nonvisible damage. The curves, which were calculated with Eq. (10), were dashed to indicate nonvisible damage, $p_c < 705$ MPa, and solid to indicate visible damage, $p_c \geq 705$ MPa. The predictions and tests are in reasonably good agreement, even when damage was visible. In Figs. 3 and 5, $F_{\max}$ was overestimated and r_c was underestimated when damage was visible. Perhaps these discrepancies combine to offset the neglect of damage in calculating the internal stresses.

Values of S_{xf} calculated with Eq. (10) are plotted against KE_{eff} as solid curves in Fig. 14 for hemispherical diameters ranging from 6.3 to 102 mm. Again, the values of S_{xf} were divided by F_{tu}. For a given value of R_1, the value of r_c increases with increasing KE_{eff}. The calculations were terminated at the lower ends of the dashed curves when r_c reached R_1. (Values of $r_c > R_1$ are physically unrealizable.) The locus of S_{xf} values for $p_c = 490$ and 705 MPa are plotted as dashed curves. These curves represent the thresholds for damage initiation and for nonvisible damage, respectively, and divide the graph into regions of no damage, nonvisible damage, and visible damage. If the FWC must have sufficient strength to accommodate nonvisible damage, then the allowable stress must not be above the lower dashed curve for all possible values of KE_{eff}. All visible damage, which would result in even lower strengths, would have to be detected and repaired.

The hemisphere diameter $2R_1$ is plotted against KE_{eff} in Fig. 15 for the values of p_c that correspond to the thresholds for initiating damage and for nonvisible damage in Fig. 14. As in Fig. 14, the curves divide the graph into regions of no damage, nonvisible damage, and visible damage. Combinations of R_1 and KE_{eff} in the "no damage" region do not cause damage, similarly for the "nonvisible damage" and "visible damage" regions. Along the curves for damage initiation and nonvisible damage, KE_{eff} increases approximately with R_1^3. Thus, for large R_1, very large values of KE_{eff} are necessary to initiate damage and to cause visible damage. But as shown in Fig. 7, the depth of nonvisible and visible damage can be nearly equal for 12.7- and 25.4-mm-diam hemispheres for the same value of KE_{eff}. Test data for the 12.7- and 25.4-mm-diam hemispheres are plotted in Fig. 15 for comparison. The filled and empty symbols differentiate between visible and nonvisible damage. The calculations and tests agree quite well.

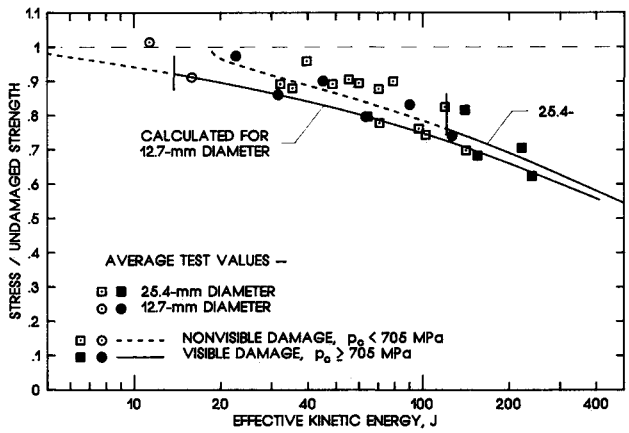

Fig. 13 Effect of hemisphere diameter on stress for first-ligament failure.

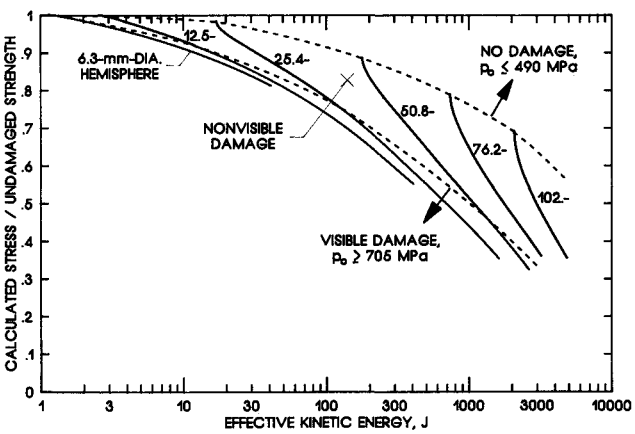

Fig. 14 Calculated stress for first-ligament failure for various hemisphere diameters.

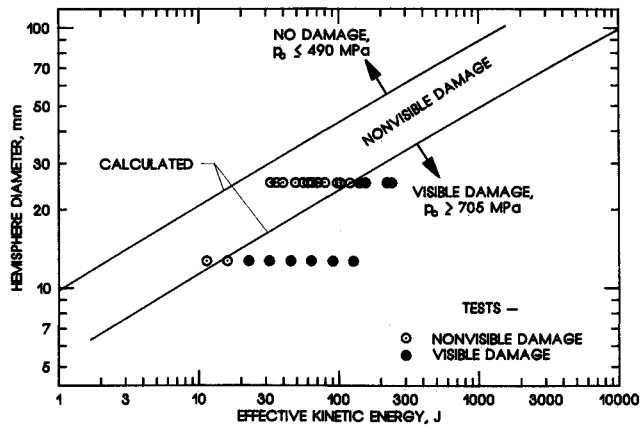

Fig. 15 Hemisphere diameter and effective kinetic energy to cause damage.

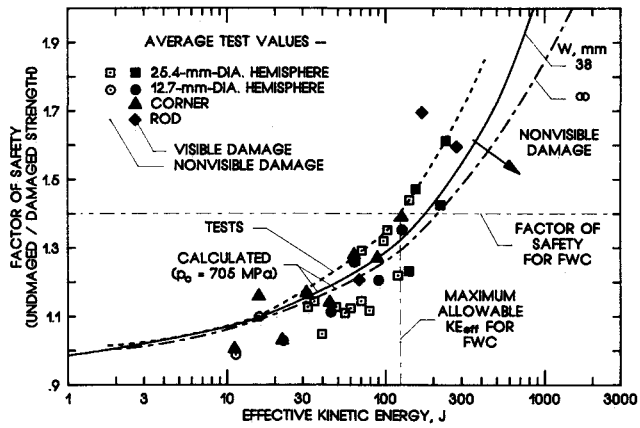

Fig. 16 Factor of safety for nonvisible damage vs effective kinetic energy.

The factor of safety for impact damage is given by the ratio of undamaged strength to damaged strength. Reciprocals of the strength ratios for the test data in Fig. 9 are plotted against KE_{eff} in Fig. 16. The reciprocal of the dashed curve for $p_c = 705$ MPa in Fig. 14 is also plotted. This curve corresponds to a factor of safety for nonvisible damage. The solid curve passes through the midst of the data and below some of the open symbols for the 25.4-mm-diam hemisphere. The dashed curve was drawn through the locus of highest open symbols using the solid curve as a guide. The factor of safety for the membrane of the FWC, which was 1.4, is shown as a horizontal line in Fig. 16. It intersects the dashed curve at $KE_{\text{eff}} = 123$ J. Thus, the FWC must be protected for values of $KE_{\text{eff}} > 123$ J or nonvisible damage can result in a factor of safety below 1.4.

The specimens in this investigation were 33- and 38-mm wide. The solid curve in Fig. 16 was calculated assuming that $w = 38$ mm. Differences between calculations for $w = 33$ and 38 mm were insignificant. The dash-dot curve in Fig. 16 was

calculated for $w = \infty$, which is more representative of a FWC. The difference between calculations for $w = 38$ mm and $w = \infty$ is only significant for very large values of KE_{eff} where the length of the equivalent surface crack in Eq. (10) exceeds about one-half the specimen width.

Consider that the FWCs were to have been moved many times: they were to have been manufactured at one location, shipped by truck to another site and loaded with solid propellant, and then shipped by rail to the launch site and assembled. Moreover, one empty FWC was dropped onto the floor at the manufacturing plant. Although this investigation was conducted with impacts from small objects like tools and equipment in mind, impacts between a moving FWC and some other rigid or massive object must also be considered. The longest FWCs had a mass of about 4500 kg empty and about 140,000 kg when filled with propellant. Thus, the potential energy or kinetic energy of one of these FWCs is very large when they are being moved, 44,000 J for an empty FWC lifted 1 m. The energy for a filled FWC would be 30 times that for an empty FWC. The results here can be applied directly because the velocity v_1 in Eq. (4) can be taken as the relative velocity. If the mass of the impacter and the target are very different, the effective mass is equal to the smallest of the two masses (see Eq. (5)). On the other hand, if the mass of the impacter and the target are equal, the effective mass is equal to one-half that of one of the masses. Like the rings, the effective mass of the FWC or the other object would probably be considerably less than the resting mass. Still, the values of KE_{eff} could be orders of magnitude times those considered in this investigation. From Fig. 16, the factor of safety exceeds 2 for values of KE_{eff} exceeding 2000 J. Thus, the FWCs must be handled very carefully and probably protected.

The large weight is a hazard even when a FWC is at rest. If an FWC lay on a protuberance, the protuberance would act like the indenter in a simulated impact. For the filled and empty rings, residual tension strengths were equal for impacts and simulated impacts when values of $F_{\max}$ were equal.[4,5] The weight of an empty FWC is about 44 kN, which is about as large as the largest impact forces for all of the indenters except the 25.4-mm-diam hemisphere (see Fig. 5). The weight of an FWC filled with propellant is about 30 times the weight of an empty FWC, which is much larger than the largest impact force. Thus, care must be taken not to lay FWCs on a hard protuberance.

Table 2 Deply results for impacts to full-scale FWC (DA-006)

Kinetic energy, J	Damage depth, mm	Impact force, kN	Impression depth, mm
	Corner		
14[a]	1.71	10.8	0.18
14[a]	1.28	10.3	0.23
34	2.13	17.5	1.14
68	2.13	26.1	1.52
102	3.45	31.4	—
136	4.98	36.8	2.34
203	5.41	45.6	—
271	5.41	48.5	3.61
339	5.41	56.2	3.76
	12.7-mm-diam hemisphere		
27[a]	2.13	16.8	0.15
27[a]	1.71	17.1	0.15
68	2.79	28.0	0.56
102	5.41	33.7	—
136	4.11	41.5	1.07
203	4.11	41.1	—
271	7.39	50.2	3.96
339	8.26	52.6	—
	25.4-mm-diam hemisphere		
122[a]	2.13	43.2	0.20
122[a]	1.71	43.1	0.20
136	2.79	43.4	—
203	4.11	56.4	0.25
271	4.98	64.2	0.30
407	4.11	77.4	0.46
542	4.98	87.6	0.53
678	8.48	109.0	0.58
678	5.41	103.0	0.46

[a] Visual damage threshold.

Full-Scale Tests

An actual FWC (DT-001) with damage and delaminations in critical regions was pressure tested to failure by Hercules at the end of the development program.[17,18] Based on results from the present investigation and work done by Hercules, delaminations, cuts, and impact damage were selected that were large enough to be detectable but not large enough to reduce the factor of safety below the required 1.4. In the membrane region, the delaminations were as large as 1.948 m^2 and the surface cuts were as deep as 1.1 mm. The impacts, which were sufficient to give at least barely visible damage on the surface, were made by propelling a 127-kg sled against the FWC. Three indenters were used, each with a different kinetic energy: a sharp corner with 13 J of energy, a 12.7-mm-diam hemisphere with 26 J of energy, and a 25.4-mm-diam hemisphere with 110 J of energy. The burst pressure was 10.01 MN/m^2, and the corresponding factor of safety was 1.54, about 10% greater than the required 1.4. The mean burst pressure of undamaged FWCs was slightly lower than 1.54. Thus, the damage, delaminations, and cuts had no significant effect on the burst pressure.

Before the test of DT-001, another FWC (DA-006) was impacted using the sled to determine appropriate impact energies. Specimens that each contained an impact site were cut from the FWC and examined ultrasonically, and then deplied. Pertinent deply results are given in Table 2.

The "visual damage threshold" (VDT), which was defined in terms of depth of indenter impression, was determined in ancillary tests to be 0.13 mm. The impact energies for DA-006 were selected so that all damage would be visible by this criteria. To verify the VDT, several teams of quality assurance personnel examined DA-006; each team discovered all the impact sites.

Recall that the uniaxial tension strength in the present investigation was reduced 30% by barely visible damage from the 25.4-mm-diam hemisphere and 10% by that from the 12.7-mm-diam hemisphere. Thus, the full-scale results and those in the present investigation seem to be in conflict. The VDTs in the present tests are summarized in Table 3.

For the visible damage thresholds in Tables 2 and 3, the effective kinetic energies in the present tests are almost the same as the kinetic energies in the DA-006 tests; however, the impact forces in the present tests are nearly twice those in the DA-006 tests for the hemispherical indenters. Thus, the effective kinetic energies in the DA-006 tests are about one-fourth of the kinetic energies, indicating that the effective mass of the FWC is only about one-third of the mass of the sled. For the 25.4-mm-diam hemisphere, a kinetic energy of nearly 542 J is required in the DA-006 tests to give the same impact force as

Table 3 Results for visible damage threshold in present tests (0.762-m-diam cylinder)

Indenter type	Effective kinetic energy, J	Damage depth in radiographs, mm	Impact force, kN
Corner	11	2.0–3.7	10–11
12.7-mm-diam hemisphere	23	0.5–2.0	23–28
25.4-mm-diam hemisphere	147	4.0–5.1	79–86

that in the present tests. That energy resulted in an impression depth of 0.53 mm. Depths were not measured in the present tests. Assuming that a given impact force would cause the same impression in the full scale and present tests, impressions as deep as 0.53 mm in the present tests were likely not considered to be visible. Because the impact forces were much greater in the present tests than in the DA-006 tests for a given kinetic energy, the damage depths were much greater, and the residual strengths were lower in the present tests than in the DA-006 tests. Had the same impression-depth criteria been used in analyzing the present test data, the strength reductions due to nonvisible damage for the present tests and the DA-006 tests would probably be in agreement. Thus, the difference between strengths for 0.13- and 0.53-mm-deep impressions indicate that residual strengths are quite sensitive to impression depth.

The FWC design was primarily governed by internal pressure and limited elongation between the attach points. The booster motors are also subjected to bending when the main engines of the Space Shuttle orbiter ignite, causing relatively large compression stresses in the aft FWCs. Marshall Space Flight Center tested in bending an FWC with a delamination and porosity larger than that allowed by accept/reject criteria. It failed prematurely at a load corresponding to a factor of safety between 1.2 and 1.3. On the other hand, two FWCs that satisfied the accept/reject criteria were loaded in bending to failure by Hercules.[19,20] The factors of safety corresponding to failure were 1.68 and 1.73. Thus, anomalous compression loads must be considered in the fracture control plan for a composite motor case.

Concluding Remarks

An investigation was made to determine the effect of low-velocity impacts by tools and small equipment on the tension strength of a thick filament-wound case (FWC) for the booster motors of the Space Shuttle. Falling weight impact tests were conducted on rings (short cylinders) that were 30.5-cm long and 36-mm thick (actual thickness of an FWC). The rings were cut from a 2.13-m-long cylinder that was wet wound on a 76.2-cm-diam mandrel using AS4 graphite fibers and an epoxy resin. Some rings were filled with inert solid propellant. Three indenters (tups) were used for the impact tests: a sharp corner and two hemispheres, one hemisphere with a 12.7-mm diameter and one with a 25.4-mm diameter. Drop height was varied and, for the 25.4-mm-diam hemisphere, mass was also varied. The rings were impacted numerous times around the circumference and then cut into 51-mm-wide tension specimens, each containing an impact site. The damage was always local to the impact site and never extended into neighboring impact sites. Because no rings remained, impacts with a 6.3-mm-diam rod were simulated by quasistatically pressing the rod against the face of surplus specimens that had been cut earlier from an empty ring. The size of damage and residual tension strength were measured.

For the hemispheres, the indentation and contact radius were well represented as Hertzian contact. Assuming Hertzian contact and Newtonian mechanics, a relationship was derived for maximum impact force, effective kinetic energy, and stiffness of the composite ring. The effective kinetic energy accounts for the relative mass of the impacter and composite ring. This relationship modeled the maximum impact force for the hemispherical indenters quite well except when the impacts made visible surface damage (indenter impressions). Even then, the effective kinetic energy gave good correlation between maximum impact forces for the empty and filled rings. The presence of the solid propellent significantly increased the mass of the FWC and elevated the impact force for a given kinetic energy.

Impact tests of an actual FWC using a massive sled also verified that decreasing the relative mass of the FWC significantly reduces the impact force for a given kinetic energy. The damage caused by the hemispheres initiated below the surface before it became visible on the surface. For both hemispheres, the damage initiated when the contact pressure exceeded 490 MPa but did not become visible on the surface until the pressure exceeded 705 MPa. The damage below the surface consisted of broken fibers and shear cracks in the epoxy. The effective kinetic energy to initiate damage below the surface and to cause visible surface damage increased with the diameter of the hemisphere. For the corner and rod, contact pressures were very large and damage was always visible on the surface. Even so, the effective kinetic energy gave good correlation between maximum impact forces for the empty and filled rings. These results were verified by tests of an actual FWC.

Under uniaxial tension load in the hoop direction, specimens with very shallow damage (only in the outermost helical layers) failed catastrophically without significant reduction in strength. But, with damaged hoop layers, the specimens failed in two stages: first, the outermost damaged layers failed and delaminated, and then, with increasing load, the remaining ligament failed. For a given value of effective kinetic energy, the residual strengths did not vary significantly with indenter shape even though the detectability of the damage did vary significantly with indenter shape. The maximum reduction in tension strength for nonvisible damage increased with increasing diameter of the hemisphere. For the 12.7- and 25.4-mm-diam hemispheres, the reductions in tension stress for first-ligament failure were about 10 and 30%, respectively, for nonvisible damage. Thus, the largest hemisphere was the most critical indenter for reducing strength with nondetectable damage.

Using the maximum impact force, the depth of impact damage caused by the hemispheres was calculated assuming Hertzian contact and a maximum shear stress criterion. Internal stresses were calculated using Love's solution for an isotropic semi-infinite body. The impact damage was represented as a semi-circular surface crack with the same depth as impact damage. Residual tension strengths were then calculated using surface crack analysis. The calculated and test values of residual tension strength were in good agreement, even when the impacts made visible damage.

The factor of safety for the membrane of a FWC was 1.4. For the worst nonvisible damage, this factor of safety corresponds to a value of effective kinetic energy of 123 J. Assuming that the factor of safety of 1.4 must account for nonvisible damage, the FWC must therefore be protected for values of $KE_{\text{eff}} > 123$ J.

The large mass of an FWC is also a hazard because of the potential for an accident when an FWC is being moved. In such an accident, KE_{eff} could easily exceed 123 J by orders of magnitude. The large mass is a hazard even when an FWC is at rest. If an FWC lay on a hard protuberance such as one of the indenters in this investigation, the FWC could be damaged and the tension strength seriously reduced. Thus, great care must be taken when an FWC is placed in a cradle or rigged for moving.

The reduction in strength due to nonvisible damage is very sensitive to the inspection criteria. Subsequent to the present investigation, impact damage associated with indenter impressions less than 0.23-mm deep was shown to cause a negligible reduction in burst pressure of an actual FWC. It was demonstrated that impressions with depths greater than 0.13 mm could be found reliably. The impressions for nonvisible damage in the present study were probably as deep as 0.5 mm.

Appendix

The term n_0 in Hertz's equation[13] is defined as

$$n_0 = (4/3)(k_1 + k_2)^{-1} \tag{A1}$$

where

$$k_1 = (1 - \nu_1^2)E_1^{-1}$$

$$k_2 = \tfrac{1}{2} A_{22}^{\frac{1}{2}} \left\{ \left[(A_{11}A_{22})^{\frac{1}{2}} + G_{zr} \right]^2 - (A_{12} + G_{zr})^2 \right\}^{\frac{1}{2}} \times G_{zr}^{-\frac{1}{2}} (A_{11}A_{22} - A_{12}^2)^{-1}$$

$$A_{11} = E_z \left[1 - 2\nu_{rz}^2 E_z E_r^{-1} (1 - \nu_r)^{-1} \right]^{-1}$$

$$A_{22} = A_{11}(E_r E_z^{-1} - \nu_{rz}^2)(1 - \nu_r^2)^{-1}$$

$$A_{12} = A_{11}\nu_{rz}(1 - \nu_r)^{-1}$$

The E_1 and ν_1 are the elastic constants of an isotropic sphere and the E_r, E_z, G_{zr}, ν_r, and ν_{rz} are the elastic constants of a transversely isotropic semi-infinite body in polar coordinates.

References

[1]Loyd, B. A., and Knight, G. K., "Impact Damage Sensitivity of Filament-Wound Composite Pressure Vessels," *1986 JANNAF Propulsion Meeting,* CPIA Pub. 455, Vol. 1, Laurel, MD, Aug. 1986, pp. 7–15.

[2]Poe, C. C., Jr., Illg, W., and Garber, D. P., "A Program to Determine the Effect of Low-Velocity Impacts on the Strength of the Filament-Wound Rocket Motor Case for the Space Shuttle," NASA TM-87588, Sept. 1985.

[3]Poe, C. C., Jr., Illg, W., and Garber, D. P., "Hidden Impact Damage in Thick Composites," *Review of Progress in Quantitative Nondestructive Evaluation,* Vol. 5B, Plenum Press, New York, 1986, pp. 1215–1225.

[4]Poe, C. C., Jr., Illg, W., and Garber, D. P., "Tension Strength of a Thick Graphite/Epoxy Laminate after Impact by a ½-In.-Radius Impacter," NASA TM-87771, July 1986.

[5]Poe, C. C., Jr., and Illg, W., "Strength of a Thick Graphite/Epoxy Rocket Motor Case After Impact by a Blunt Object," *Test Methods for Design Allowables for Fibrous Composites,* edited by C. C. Chamis, American Society for Testing and Materials, ASTM STP 1003, Philadelphia, PA, 1989, pp. 150–179 (also NASA TM-89099, Feb. 1987; and *1987 JANNAF Composite Motor Case Subcommittee Meeting,* CPIA Pub. 460, Feb. 1987, pp. 179–202).

[6]Poe, C. C., Jr., "Surface Crack Analysis Applied to Impact Damage in a Thick Graphite/Epoxy Composite," *Surface Crack Growth: Models, Experiments and Structures,* edited by W. G. Reuter, J. H. Underwood, and J. C. Newman, Jr., American Society for Testing and Materials, ASTM STP 1060, Philadelphia, PA, 1990, pp. 194–212 (also NASA TM-100600, April 1988).

[7]Harris, C. E., and Morris, D. H., "Preliminary Report on Tests of Tensile Specimens with a Part-Through Surface Notch for a Filament-Wound Graphite/Epoxy Material," NASA CR-172545, March 1985.

[8]Madaras, E. I., Poe, C. C., Jr., Illg, W., and Heyman, J. S., "Estimating Residual Strength in Filament Wound Casings from Non-Destructive Evaluation of Impact Damage," *Review of Progress in Quantitative Nondestructive Evaluation,* Vol. 6B, Plenum Press, New York, 1987, pp. 1221–1230.

[9]Madaras, E. I., Poe, C. C., Jr., and Heyman, J. S., "Combining Fracture Mechanics and Ultrasonics NDE to Predict the Strength Remaining in Thick Composites Subjected to Low-Level Impact" *1986 Ultrasonics Symposium Proceedings,* edited by B. R. McEvoy, Vol. 86CH2375-4, No. 2, Inst. of Electrical and Electronic Engineers, New York, 1987, pp. 1051–1059.

[10]Madaras, E. I., Poe, C. C., Jr., and Heyman, J. S., "A Non-destructive Technique for Predicting the Strength Remaining in Filament Wound Composites Subjected to Low-Level Impact," *1987 JANNAF Composite Motor Case Subcommittee Meeting,* CPIA Pub. 460, Laurel, MD, Feb. 1987, pp. 249–258.

[11]Poe, C. C., Jr., "Simulated Impact Damage in a Thick Graphite/Epoxy Laminate Using Spherical Indenters," *Proceedings of American Society for Composite Materials,* Technomic Publishing, Lancaster, PA, Nov. 1988 (also NASA TM-100539, Jan. 1988).

[12]Poe, C. C., Jr., "Relevance of Impacter Shape to Nonvisible Damage and Residual Tensile Strength of a Thick Graphite/Epoxy Laminate," NASA TM-102599, April 1990.

[13]Greszczuk, L. B., "Damage in Composite Materials Due to Low Velocity Impact," *Impact Dynamics,* Wiley, New York, 1982, pp. 55–94.

[14]Chatterjee, S. N., "Surface Cracks in Thick Laminated Fiber Composite Plates," *Surface Crack Growth: Models, Experiments and Structures,* edited by W. G. Reuter, J. H. Underwood, and J. C. Newman, Jr., American Society for Testing and Materials, ASTM STP 1060, Philadelphia, PA, 1990, pp. 177–193.

[15]Love, A. E. H., "The Stress Produced in a Semi-Infinite Solid by Pressure on Part of the Boundary," *Philosophical Transactions of the Royal Society of London,* Series A, Vol. 228, Nov. 1929, pp. 377–420.

[16]Newman, J. C., Jr., and Raju, I. S., "Stress-Intensity Factor Equations for Cracks in Three-Dimensional Finite Bodies," *Fracture Mechanics: Fourteenth Symposium—Volume I: Theory and Analysis,* American Society for Testing and Materials, ASTM STP 791, Philadelphia, PA, 1983, pp. I-238–I-268.

[17]Gessner, R. F., "Test Report on Hydroburst of Damage Tolerance Segment DT-001," Hercules/Votaw—A Joint Venture, Document No. FWC-01-177 (Contract No. 114010, FWC), Magna, UT, Nov. 1987.

[18]Lehr, S. L., and Madsen, C. B., "Damage Tolerance Phase II Final Report for Space Shuttle Solid Rocket Motor Filament Wound Case," Hercules Inc., Document No. FWC-01-182 (Contract No. 114010, FWC), Magna, UT, Nov. 25, 1987.

[19]Gessner, R. F., "Test Report on Fullscale Compression Test of DA-013," Hercules/Votaw—A Joint Venture, Document No. WDI-(FWC-3) FWC-01-176 (Contract No. 114010, FWC), Magna, UT, Oct. 1987.

[20]Bucinell, J., "Test Report on Fullscale Compression Test of DA-010," Hercules/Votaw—A Joint Venture, Document No. WDI-(FWC-3) FWC-01-178 (Contract No. 114010, FWC), Magna, UT, Nov. 1987.

Earl A. Thornton
Associate Editor